TriMorph: The Transformative Tricopter

J. Lee†, J-M Ingargiola‡, and S. Viollet‡*
†Department of Mechanical Engineering, Massachusetts Institute of Technology, MA, USA
‡CNRS / Aix-Marseille Université, ISM, Marseille, France

ABSTRACT

Bio-inspired robotic systems increasingly exploit morphological adaptation to operate under varying environmental constraints. While morphing mechanisms have been investigated for unmanned aerial vehicles (UAVs), relatively little attention has been given to tricopters, despite their favorable efficiency and agility characteristics. This paper presents TriMorph, a transforming tricopter capable of continuously varying its frame through a single-actuator truss mechanism. A geometric model relating actuator motion to the deploy angle is derived and incorporated into a configuration-dependent dynamic formulation. Experimental flights demonstrate consistent behavior across configurations, highlighting morphology as a control input that modifies the inertia matrix. These results suggest a pathway toward aerial robots that adapt their physical structure to changing task requirements. The prototype increases its top-down area by more than 3$\times$ and principal inertias by up to 2.9$\times$. These results demonstrate that rotational geometric morphing directly modulates the inertia matrix in flight, thereby expanding the operational envelope of tricopter UAVs.

1 INTRODUCTION

Multirotor UAVs are increasingly deployed in logistics, disaster response, agriculture, and defense applications. However, most platforms rely on fixed-geometry airframes that cannot adapt their morphology to changing environmental or task constraints. In contrast, biological flyers, such as birds, dynamically adjust wing morphology to balance agility, stability, and energy efficiency across varying conditions. Not only are these aerial creatures able to vary their aerodynamics at will with their foldable wings and overlapping feathers, they are able to perform rapid adaptation and optimization suitable for hunting, fleeing and energy efficiency [1]. By integrating characteristics of wildlife, drones would be able to navigate through narrow openings needed for search and rescue, rapidly adapt to atmospheric conditions, optimize energy consumption, and minimize radio wave reflections for military stealth, to name a few examples. Although there exists research on this topic with transforming drones [2], [3], [4], tricopters, unlike other multirotor designs, offer speed and agility ([5]). TriMorph takes the leap in bringing our rigid aerial vehicles one step closer to the functionalities of flying animals, while retaining the strength and robust qualities of a drone. The main contributions of this work are the design of a morphing tricopter architecture, dynamic modeling that captures configuration-dependent behavior, and a control implementation enabling flight.

*Email address: stephane.viollet@cnrs.fr

Figure 1: TriMorph expansion evolution.

2 RELATED WORK

Although similar shape-shifting drones have been developed [2], [4], [6], [7], [8], [9], [10] the degree of their transformations is often limited to one arm actuated movements, limiting their expansion and therefore, range of adaptation. For example, in [2], the fully expanded and contracted states of the 'Foldable Drone' are targeted for object inspection and crevice navigation and are not suitable for extreme changes in environmental conditions, where rapid change in drone dynamics is necessary while maintaining stability. On the other hand, Morpho-Copter [4] is only able to change the angle of its arms, and its four servo motors make it prone to failures, according to the authors. As for the sliding arm quadcopter [7], it changes its shape through arm extensions, consequently moving its center of mass; however, this design also does not change its rotational inertia significantly, as seen from its minimal pitch and yaw rotations.

Given the complexity of current morphing drones, with numerous servo motors, the drones do not achieve large increases in width, which is why TriMorph utilizes truss-like mechanisms to simplify the servo motor complexity while maximizing adaptation and stability with expansion [11]. Figure 1 illustrates the expansion evolution of TriMorph from its compact configuration to its fully deployed state, highlighting the continuous change in planform area span.

To contextualize the performance indices of TriMorph against prominent platforms in the literature, a comparative overview is provided in Table 1.

Table 1: Comparative analysis of TriMorph against state-of-the-art morphing UAVs.

Platform	**Type**	**Morphing Actuators**	**Expansion Ratio (Area / Span)**	**Inertia Modulation Factor (L_{zz})**	**CoG Shift During Flight**
Foldable Drone [2]	Quadrotor	4 Servos	$\sim 1.2\times$ (Area)	Low	Negligible
Morpho-Copter [4]	Quad-Bi	4 Servos	$\sim 1.2\times$ (Area)	Low	Negligible
Sliding Arm Quad [7]	Quadrotor	2 Servos	$\sim 1.2\times$ (Span)	Minimal (xy only)	Pronounced
TriMorph	**Tricopter**	**1 Servo**	$> 3.2\times$ **(Area)**	**Up to** $2.9\times$	**Negligible** (< 0.8 **mm**)

Figure 1 illustrates the expansion evolution of TriMorph from its compact configuration to its fully deployed state, highlighting the continuous change in planform area span.

3 MECHANICAL DESIGN

3.1 Truss-Based Morphing Architecture

Many morphing UAVs rely on multiple actuators and rigid telescoping arms, increasing mass and mechanical complexity [11]. In contrast, TriMorph adopts a planar truss-inspired mechanism in which each arm behaves primarily as a two-force member. This allows structural loads to be carried predominantly in axial tension or compression rather than in bending, supporting lightweight construction while maintaining stiffness.

All twelve joints were manufactured in carbon-fiber reinforced polymer (PET-CF) using additive manufacturing. The truss layout ensures that the geometric expansion modifies the motor to centroid distance without introducing large off-axis bending loads in the members.

3.2 Joint Geometry and Stress Distribution

Arm connections experience the highest stresses in the structure because they transfer load between members while undergoing repeated rotation during morphing. Early prototypes exhibited fracture at the arm roots due to localized bending stresses. To mitigate this, the joints were redesigned with enlarged circular ends, increasing the load transfer area and reducing stress concentration. The peak stress at a geometric discontinuity is governed by:

$$\sigma_{\max} = K_t \sigma_{\text{nom}} \tag{1}$$

where K_t is the stress concentration factor. By replacing narrow rectangular ends with circular profiles, K_t is reduced, distributing load more uniformly into the arm body.

Additionally, the pin connection introduces bearing stress:

$$\sigma_b = \frac{F}{t d_p} \tag{2}$$

where t is the material thickness and d_p the pin diameter. Increasing the joint diameter increases the projected bearing area, lowering local compressive stresses and reducing crack initiation in the printed composite layers. This is particularly important for layer-wise printed polymers, which are susceptible to delamination under localized transverse loading. As a result, the rounded joint geometry significantly improved durability and prevented brittle fracture during repeated morphing cycles.

3.3 Primary Arm Bending Stiffness

The arm connecting the rotating frame to the motor experiences a different loading than the remaining members. Although most truss elements primarily carry axial forces, the motor arm acts as a cantilever beam that supports rotor thrust, gyroscopic torques, and inertial loads during maneuvering. Consequently, bending stress dominates its structural loading. To increase stiffness without significantly increasing mass, the motor arm was printed with twice the vertical height of the other arms. The bending stress in a beam is given by:

$$\sigma = \frac{Mc}{I} \tag{3}$$

where M is the bending moment, c is the distance to the outer fiber, and I is the second moment of area. For a rectangular cross-section:

$$I = \frac{bh^3}{12} \tag{4}$$

Thus, doubling the motor arm height increases I by a factor of $2^3 = 8$, and c by a factor of 2, reducing bending stress and deflection by factors of 4 and 8 respectively for the same loading. This modification significantly improved structural rigidity and reduced oscillations at the motor mount during flight, while adding minimal mass compared to uniformly thickening all members.

3.4 Low-Friction Rotational Interfaces

Rotational joints use $2\,\text{mm}$ PTFE spacers to reduce mass and avoid stick–slip during repeated morphing. PTFE exhibits very low surface energy and shear strength, producing a friction coefficient of approximately $\mu \approx 0.04$–0.10 against the carbon-fiber composite. The material also conforms slightly to surface irregularities, distributing contact pressure and limiting abrasive wear at the joint interface. This allowed smooth expansion and contraction without mechanical binding or observable wear during testing.

3.5 Actuation Strategy

Instead of a conventional tail tilt mechanism, TriMorph employs a coaxial motor unit in which counter-rotating propellers balance the net reaction torque generated by the propellers. A single servo rotates the top triangular plate, driving the truss mechanism and changing the radial motor distance.

The expansion angle α directly modifies TriMorph's frame and inertia while maintaining symmetry about the body z-axis. Because angular acceleration scales as:

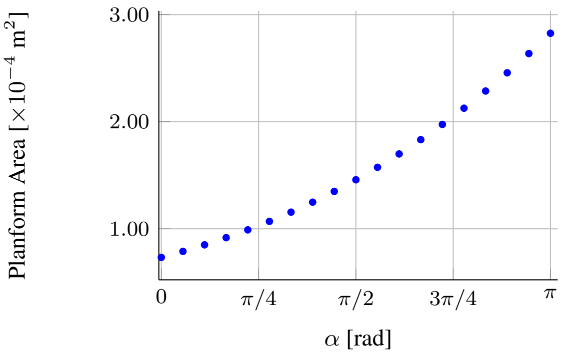

Figure 2: Planform Area *vs*. Deploy Angle (α), proportional to kx^2, where $k \in \mathbb{R}$.

$$\dot{\omega} = J^{-1}\tau \tag{5}$$

increasing the moment of inertia reduces angular acceleration for a given torque, improving disturbance resilience, while the compact configuration enables greater agility.

Through serial radio communication, we implemented a toggle that allows the drone to expand and contract mid-air. At an initial configuration, its planform area, defined by the equilateral triangle formed by the three motor hubs vertex-to-vertex, is $7{,}317.352\ \mathrm{mm}^2$. TriMorph is capable of expanding to more than triple its original area to $23{,}482.812\ \mathrm{mm}^2$. This relationship is depicted in Figure 2, where the planform area is plotted as a function of the deploy angle. For the principal-axis rotational inertia, the tricopter starts at $L_{xx} = 7.1 \times 10^{-4}\,\mathrm{kg\,m^2}$, $L_{yy} = 7.6 \times 10^{-4}\,\mathrm{kg\,m^2}$, $L_{zz} = 9.9 \times 10^{-4}\,\mathrm{kg\,m^2}$, and morphs to $L_{xx} = 1.7 \times 10^{-3}\,\mathrm{kg\,m^2}$, $L_{yy} = 1.6 \times 10^{-3}\,\mathrm{kg\,m^2}$, $L_{zz} = 2.9 \times 10^{-3}\,\mathrm{kg\,m^2}$.

This not only creates significant advantages in resilience to disturbances, but also enables the UAV to alter its dynamics midair in response to environmental conditions, such as air drag. Because the morphing mechanism relies entirely on a closed-loop internal truss structure driven by a single internal servo, the total mass of the vehicle remains strictly constant ($m_t = 345$ g) during adaptation. Furthermore, due to the rotational symmetry of the three-arm truss layout about the body z_b-axis, the theoretical Center of Gravity (CoG) experiences zero translation in the xy-plane ($\Delta x_G = 0, \Delta y_G = 0$). Experimentally, minor manufacturing and assembly tolerances result in a negligible CoG translation of less than 0.8 mm, which is easily rejected by the attitude controller's integral action. Finally, a custom triangular PCB board (Figure 4) is mounted on the drone to provide easily accessible integration of electronics.

4 GEOMETRIC ANALYSIS OF THE MECHANISM

We describe here the motion of one motor with respect to a rotation of the top triangular plate, hereafter referred to as the drive plate, around the vertical axis z_b by a known angle α. As shown in Figure 3, we consider the body frame $\mathcal{B} = \{O; \vec{x}_b, \vec{y}_b, \vec{z}_b\}$ to be fixed to the bottom triangular base plate. Points N and M move along a circle centered on point O and C, respectively. As such, distances ON, NM and CM are constant and named R_1, L and R_2, respectively. Similarly, point M is seen to be at the intersection of the circle centered at N with a radius L and the circle centered at C.

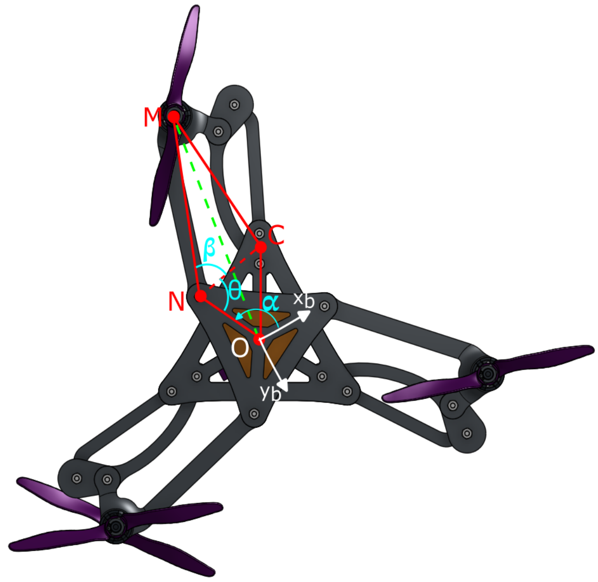

Figure 3: Diagram showing the motor's position vector dependent on drive plate rotation α and subsequent angles β and θ. The dotted green line represents the distance d. The body frame is considered attached to the bottom triangular base plate.

By definition, we have:

$$\overrightarrow{ON} = \begin{bmatrix} x_N \\ y_N \end{bmatrix} = R_1 \begin{bmatrix} \cos\alpha \\ \sin\alpha \end{bmatrix} \tag{6}$$

Let NC be the distance between the centers: $NC = \sqrt{(x_N - x_C)^2 + (y_N - y_C)^2}$, with x_c and y_c known by construction. In the triangle $\triangle NCM$, we know all three sides: L, R_2, and NC. Given this, we can find the internal angle at N (named β) using the law of cosines:

$$\cos(\beta) = \frac{NC^2 + L^2 - R_2^2}{2 \cdot NC \cdot L} \tag{7}$$

Then, the coordinates of M are simply a rotation and translation from point N. The angle of the vector $\overrightarrow{NC}$ relative to the x-axis is: $\theta = \operatorname{atan2}(y_N - y_C, x_N - x_C)$. Finally, we have the coordinates of M:

$$x_M = x_N + L\cos(\theta + \beta) \tag{8}$$
$$y_M = y_N + L\sin(\theta + \beta) \tag{9}$$

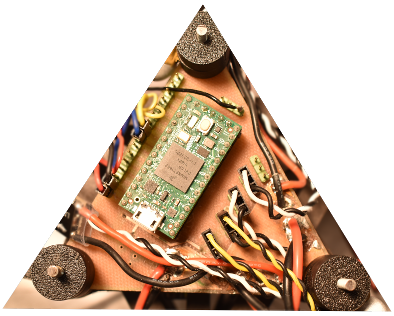

Figure 4: Custom-made triangular PCB board supporting the Teensy 4.0 board running the dRehmFlight autopilot [12].

The distance d_i (norm of $\overrightarrow{OM_i}$) between the motor M_i and O is $\sqrt{x_{Mi}^2 + y_{Mi}^2}$ and the orientation of $\overrightarrow{OM_i}$ is named $\theta_{M_i} = \text{atan2}(y_{Mi}, x_{Mi})$ with $i \in [1, 3]$. This distance, modeled by a four-bar (crank-rocker) mechanism, can be approximated as a single-bar mechanism. We measured an error as small as 2.2% between the real and theoretical distances d for three α angles (0°, 90° and 180°). Therefore, we treat R_2 as constant in the simplified model. The theoretical geometry was simulated with Geogebra software.

5 DYNAMICAL MODEL

In this section, we develop the equations of motion (EOMs) for TriMorph using the classical Newton-Euler framework. Because the tricopter undergoes geometric morphing, the distance d_i between each motor M_i and the body center varies with the drive plate angle α. Figure 5 illustrates the compact configuration at $\alpha = 0°$, corresponding to the minimum motor-to-center distance d_i. Figure 6 shows the fully deployed configuration at $\alpha = 180°$, corresponding to the maximum radial extension of the motors and increased rotational inertia.

5.1 *Forces and Torques*

The forces and drag torques produced by each rotor are assumed to be proportional to the square of the angular speeds ω_i: $f_i = k_t\omega_i^2$ and $\tau_i = (-1)^i k_d \omega_i^2 \quad \forall i \in \{1, 2, 3, 4\}$. The force produced by the i^{th} rotor is thus:

$$\boldsymbol{f}_i = \begin{bmatrix} 0 \\ 0 \\ -k_t\omega_i^2 \end{bmatrix} \text{ and } \mathbf{F}_m^b = \begin{bmatrix} 0 \\ 0 \\ -k_t\left(\omega_1^2 + \omega_2^2 + \omega_{3,4}^2\right) \end{bmatrix} \tag{10}$$

Motors 3 and 4 are aligned, so the thrust is distributed fifty-fifty between the two motors. Because the rotors maintain a strictly perpendicular thrust orientation relative to the horizontal base plate throughout the morphing process, the total static thrust required to maintain a steady hover remains uniform across the full expansion range. Further experiments will be achieved to measure changes in power consumption when transitioning from the compact ($\alpha = 0°$) to the fully deployed state ($\alpha = 180°$), primarily caused by minor variations in downstream airflow interaction with the expanded structural frame.

Let (M_1, M_2, M_3) be the application points of the forces (f_1, f_2, f_3) respectively. Then the torque generated by the rotors with respect to the center of mass G can be expressed in the body frame as:

$$\mathbf{T}_r^b = \sum_{i=1}^{3} \boldsymbol{\tau}_{m,i}^b = \sum_{i=1}^{3} (\mathbf{G}_{Mi} \times \boldsymbol{f}_i) \tag{11}$$

where G_{Mi} is the vector of the distance of the i^{th} rotor from the center of gravity G defined as follows (Figure 3):

$$\mathbf{G} = \begin{bmatrix} | & | & | \\ \mathbf{G}_{M_1} & \mathbf{G}_{M_2} & \mathbf{G}_{M_3} \\ | & | & | \end{bmatrix} = \begin{bmatrix} d\cos\theta_{M1} & d\cos\theta_{M2} & -d\cos\theta_{M3} \\ d\sin\theta_{M1} & -d\sin\theta_{M2} & d\sin\theta_{M3} \\ 0 & 0 & 0 \end{bmatrix} \tag{12}$$

Then, we can apply equations 12 to 11 to express the torque produced by the rotors as:

$$\mathbf{T}_r^b = \begin{bmatrix} dk_t\left(-\omega_1^2\sin(\theta_{M1}) + \omega_2^2\sin(\theta_{M2}) - \omega_{3,4}^2\sin(\theta_{M3})\right) \\ dk_t\left(\omega_1^2\cos(\theta_{M1}) + \omega_2^2\cos(\theta_{M2}) - \omega_{3,4}^2\cos(\theta_{M3})\right) \\ 0 \end{bmatrix} \tag{13}$$

where we consider $d_1 = d_2 = d_3 = d$ and $(\omega_3^2 + \omega_4^2) = \omega_{3,4}^2$.

In addition to thrust-induced reaction torques, each rotor generates an aerodynamic drag torque about the body z-axis, opposing its direction of rotation. The total drag torque from the four rotors is therefore given by:

$$\mathbf{T}_d^b = \begin{bmatrix} \tau_x \\ \tau_y \\ \tau_z \end{bmatrix} = \begin{bmatrix} 0 \\ 0 \\ -k_d\left(-\omega_1^2 + \omega_2^2 - \omega_3^2 + \omega_4^2\right) \end{bmatrix} \tag{14}$$

By grouping equations 10, 13 and 14, the expression for the total forces and torques described by the tricopter control mixer is obtained by:

$$\begin{bmatrix} F_x \\ F_y \\ F_z \\ \tau_x \\ \tau_y \\ \tau_z \end{bmatrix} = \begin{bmatrix} \mathbf{F}_m^b \\ \mathbf{T}_r^b + \mathbf{T}_d^b \end{bmatrix} \tag{15}$$

5.2 *Rigid Body Model*

TriMorph is modeled as a rigid body of mass m_t. The propulsive force $\mathbf{F}_m^b$ is expressed in the body frame and transformed into the inertial (earth) frame for translational dynamics.

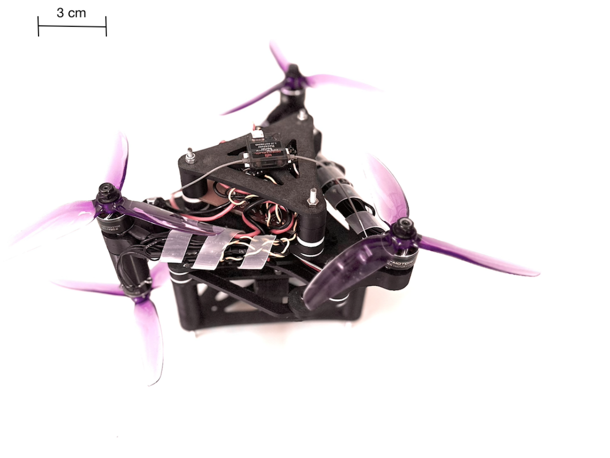

Figure 5: TriMorph in its most compact state at a drive plate rotation of 0°.

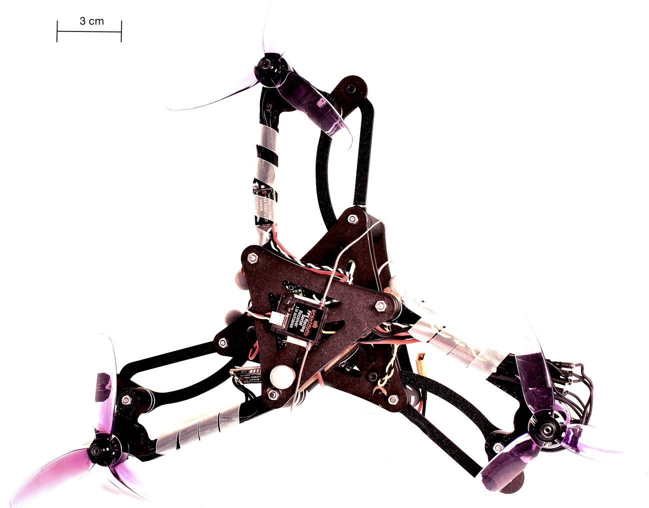

Figure 6: TriMorph in its fully deployed state at a drive plate rotation of 180°.

The gravitational force acting on the vehicle is given in the inertial frame as:

$$\mathbf{F}_g^e = \begin{bmatrix} 0 \\ 0 \\ m_t g \end{bmatrix}. \tag{16}$$

The translational dynamics are subjected to a configuration-dependent bluff-body aerodynamic drag force, where the effective drag profile scales proportionally with the planform area expansion shown in Figure 2. This might yield a highly streamlined, high-speed profile in the compact configuration and a high-drag, high-stability profile when fully expanded. This point remains to be shown in further experiments involving a windshaper.

We define $\boldsymbol{\xi}^e \triangleq \begin{bmatrix} x & y & z \end{bmatrix}^\top, \boldsymbol{\eta}^b \triangleq \begin{bmatrix} \phi & \theta & \psi \end{bmatrix}^\top$ and $\boldsymbol{\omega}^b \triangleq \begin{bmatrix} \omega_p & \omega_q & \omega_r \end{bmatrix}^\top$. Using the Newton-Euler framework, the translational dynamics of the tricopter is:

$$\ddot{\boldsymbol{\xi}}^e = \frac{1}{m_t}\left[\boldsymbol{R}_e^b(\boldsymbol{\eta})^\top \mathbf{F}_m^b + \mathbf{F}_g^e\right] \tag{17}$$

$$\dot{\boldsymbol{\eta}} = \boldsymbol{\Gamma}(\boldsymbol{\eta})^{-1}\boldsymbol{\omega}^b \tag{18}$$

$$\dot{\boldsymbol{\omega}}^b = \mathbf{J}^{-1}\left[\left(-\boldsymbol{\omega}^b \times \mathbf{J}\boldsymbol{\omega}^b\right) + \mathbf{T}_m^b\right] \tag{19}$$

with $\mathbf{J}$ the inertia matrix, the rotation matrix $\boldsymbol{R}_e^b = \boldsymbol{R}_x(\phi)\boldsymbol{R}_y(\theta)\boldsymbol{R}_z(\psi)$ and $\boldsymbol{\Gamma}(\boldsymbol{\eta})$ given by:

$$\boldsymbol{\Gamma}(\boldsymbol{\eta}) = \begin{bmatrix} 1 & 0 & -\sin\theta \\ 0 & \cos\theta & \sin\phi\cos\theta \\ 0 & -\sin\phi & \cos\phi\cos\theta \end{bmatrix} \tag{20}$$

6 CONTROL IMPLEMENTATION

The flight control system is based on the open-source dRehmFlight VTOL architecture [12]. The controller runs on a Teensy 4.x microcontroller (Figure 4) at loop frequencies exceeding 2 kHz, enabling low-latency attitude stabilization. For the tricopter configuration, a custom control mixer was developed to accommodate asymmetric thrust geometry and decouple yaw dynamics from roll and pitch. The pitch and roll PID outputs are distributed across the four primary lifting motors, while yaw control is handled independently to mitigate non-linear coupling effects introduced by the morphology. As shown in Figure 7, the control pipeline consists of state estimation, command mapping, attitude control and morphology-aware mixing.

6.1 State Estimation

Attitude is estimated using an IMU-based quaternion filter. Gyroscope integration provides short-term orientation propagation while accelerometer (gravity) and magnetometer (heading) measurements provide drift correction. The estimator follows the standard form:

$$\dot{\mathbf{q}} = \frac{1}{2}\mathbf{q} \otimes \boldsymbol{\omega} - \beta \nabla J \tag{21}$$

where $\mathbf{q}$ is the attitude quaternion and β balances drift rejection and noise sensitivity. Euler angles (ϕ, θ, ψ) are derived from $\mathbf{q}$ for feedback control.

6.2 Command Mapping

User commands are mapped to normalized thrust and attitude setpoints:

$$u_T \in [0, 1] \tag{22}$$

$$\phi_d \in [-\phi_{\max}, \phi_{\max}] \tag{23}$$

$$\theta_d \in [-\theta_{\max}, \theta_{\max}] \tag{24}$$

$$r_d \in [-r_{\max}, r_{\max}] \tag{25}$$

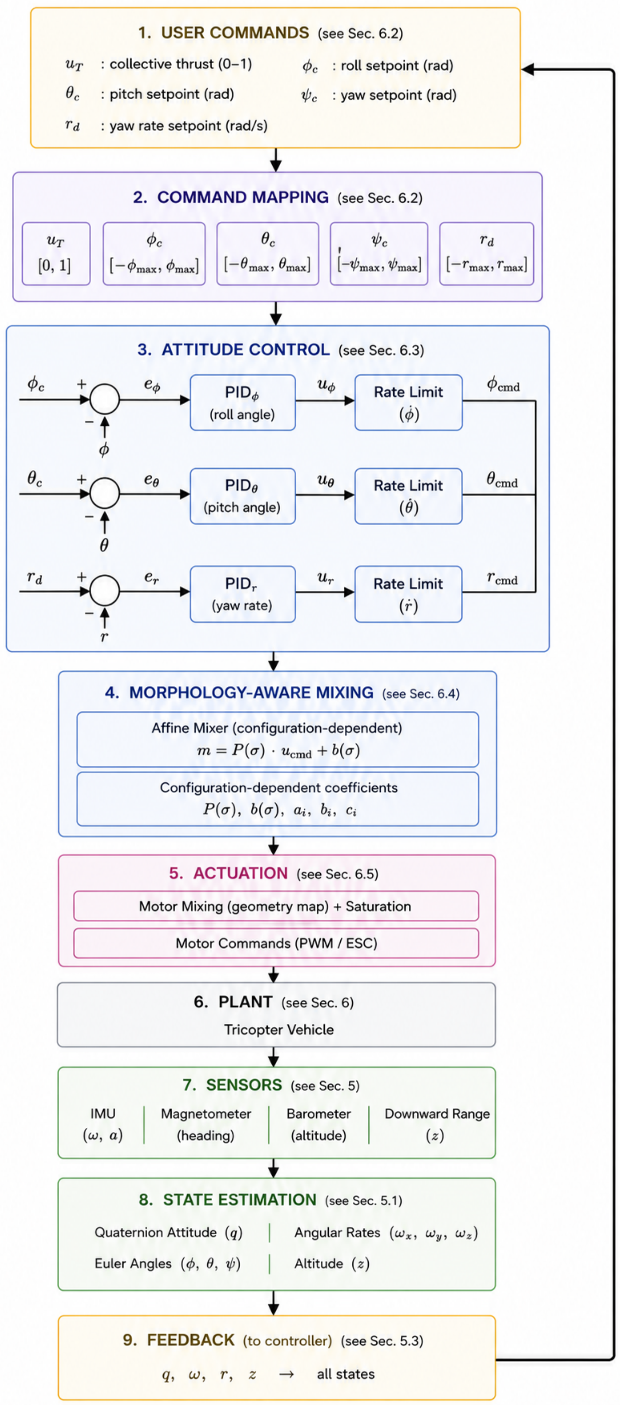

Figure 7: General control architecture of TriMorph's flight control system, showing command mapping, attitude control, configuration-dependent motor mixing, actuation, sensor feedback, and state estimation within each control cycle.

6.3 *Attitude Control*

Roll and pitch are regulated using PID control on angle error, with rate damping from gyroscope measurements:

$$e_\phi = \phi_d - \phi, \tag{26}$$

$$u_\phi = k_{p,\phi} e_\phi + k_{i,\phi} \int e_\phi dt - k_{d,\phi} \omega_x \tag{27}$$

Yaw control follows the same structure using yaw rate feedback and the integrator limiting prevents windup near zero thrust.

6.4 *Morphology-Aware Mixing*

Because the arm length d varies during morphing, the effectiveness of each rotor changes with configuration. Instead of retuning gains, we compensate using an affine mixer mapping control inputs to motor commands:

$$m_i = u_T + a_i u_\theta + b_i u_\phi + c_i u_r \tag{28}$$

where coefficients (a_i, b_i, c_i) encode configuration-dependent control authority. This allows stable flight across compact and deployed geometries without altering the high-level controller. With this flight controller, we are able to establish resilience in roll, pitch, and yaw, as the drone lifts off into hover state for the fully deployed configuration (see Figure 8).

7 CONCLUSION

In conclusion, integrating a morphing mechanism into a tricopter platform significantly enhances operational adaptability. By dynamically adjusting TriMorph's characteristic span, the vehicle transitions between a compact configuration optimized for maneuverability in confined environments and an extended configuration that improves attitude resilience and endurance during forward flight. This variable geometry enables real-time modulation of the system's moment of inertia and control authority, expanding the flight envelope beyond that of a fixed-geometry platform. When combined with the dRehmFlight VTOL control architecture, the morphing mechanism supports stable hovering flight within a single airframe. With this flight controller, we are able to implement a stable control in roll, pitch, and yaw, as the drone lifts off in its fully deployed state. Stability in intermediate states remains to be shown.

While preliminary gust rejection experiments successfully verified the immediate stability benefits of physical inertia modulation, future work will focus on extensive windshape characterization to accurately map dynamic transitions under continuous crosswind aerodynamic loading by means of a windshaper available at the lab.

ACKNOWLEDGMENT

We acknowledge the support of the Centre National de la Recherche Scientifique (CNRS), Aix-Marseille University and the Massachusetts Institute of Technology through

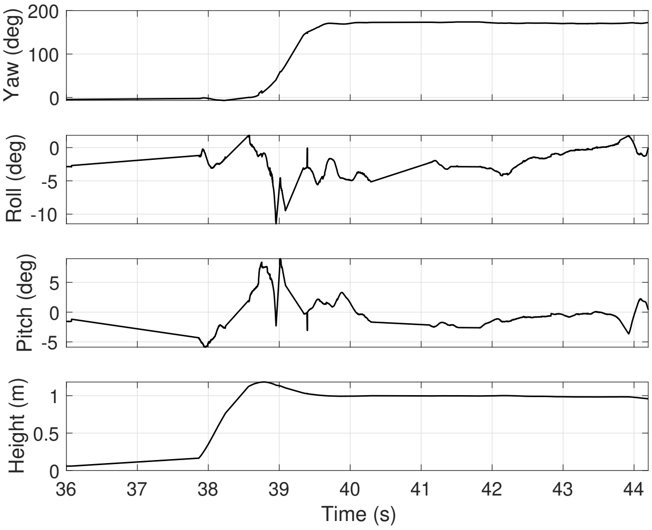

Figure 8: Experimental measurements of pitch, roll, yaw, and altitude over time before and after takeoff. The yaw response remains stable for several seconds following liftoff.

the MIT France MISTI Program. This research work was also supported by the French National Agency for Research (ANR) under the ResiRob project (ANR-24-CE33-4511-01).

REFERENCES

[1] S. Mintchev and D. Floreano. Adaptive morphology: A design principle for multimodal and multifunctional robots. *IEEE Robotics & Automation Magazine*, 23(3):42–54, September 2016.

[2] D. Falanga, K. Kleber, S. Mintchev, D. Floreano, and D. Scaramuzza. The foldable drone: A morphing quadrotor that can squeeze and fly. *IEEE Robotics and Automation Letters*, 4(2):209–216, April 2019.

[3] N. Bucki and M. W. Mueller. Design and control of a passively morphing quadcopter. In *Proceedings of the IEEE International Conference on Robotics and Automation (ICRA)*, pages 9116–9122, 2019.

[4] H. Modi, H. Su, X. Liang, and M. Zheng. Morphocopter: Design, modeling, and control of a new transformable quad-bi copter. In *Proceedings of the IEEE International Conference on Robotics and Automation (ICRA)*, June 2025.

[5] Desh Deepak Sharma, Jeremy Lin, and Ayush Singh. Disturbance observer-based adaptive sliding mode control for variable dihedral and dual-mode yaw vectoring medium-size tricopter uav. *Scientific Reports*, 2026.

[6] Ju-Hee Lee, Sumin Jung, Jinwoo Jang, Yeji Han, Minchae Kang, Jihun Seong, Suyeon Seo, Eunsol Park, Haesol Kwak, and Min-Woo Han. Design challenges to expand the functionality of drones: Deformable rotorcraft and nature-inspired flapping drones. *Advanced Intelligent Systems*, page e202500790, 2025.

[7] R. Kumar, A. Deshpande, J. Wells, and M. Kumar. Flight control of sliding arm quadcopter with dynamic structural parameters. In *Proceedings of the IEEE/RSJ International Conference on Intelligent Robots and Systems (IROS)*, October 2020.

[8] P. Pounds, R. Mahony, J. Gresham, P. Corke, and J. M. Roberts. Towards dynamically-favourable quad-rotor aerial robots. In *Proceedings of the Australasian Conference on Robotics and Automation*, 2004.

[9] V. Riviere, A. Manecy, and S. Viollet. Agile robotic fliers: A morphing-based approach. *Soft Robotics*, 2018.

[10] J. C. Gomez and E. Garcia. Morphing unmanned aerial vehicles. *Smart Materials and Structures*, 20(10):103001, 2011.

[11] David St-Onge and Clément Gosselin. Synthesis and design of a one degree-of-freedom planar deployable mechanism with a large expansion ratio. *Journal of Mechanisms and Robotics*, 8(2):021025, 2016.

[12] Nick Rehm. *dRehmFlight VTOL: Open-Source Flight Control and Stabilization*, 2020. Accessed February 2026.